

ARTICLE

Received 12 Sep 2016 | Accepted 25 Oct 2016 | Published 16 Dec 2016

DOI: 10.1038/ncomms13704

OPEN

Imaging electric field dynamics with graphene optoelectronics

Jason Horng^{1,2,*}, Halleh B. Balch^{1,2,*}, Allister F. McGuire³, Hsin-Zon Tsai¹, Patrick R. Forrester¹, Michael F. Crommie^{1,2,4}, Bianxiao Cui³ & Feng Wang^{1,2,4}

The use of electric fields for signalling and control in liquids is widespread, spanning bioelectric activity in cells to electrical manipulation of microstructures in lab-on-a-chip devices. However, an appropriate tool to resolve the spatio-temporal distribution of electric fields over a large dynamic range has yet to be developed. Here we present a label-free method to image local electric fields in real time and under ambient conditions. Our technique combines the unique gate-variable optical transitions of graphene with a critically coupled planar waveguide platform that enables highly sensitive detection of local electric fields with a voltage sensitivity of a few microvolts, a spatial resolution of tens of micrometres and a frequency response over tens of kilohertz. Our imaging platform enables parallel detection of electric fields over a large field of view and can be tailored to broad applications spanning lab-on-a-chip device engineering to analysis of bioelectric phenomena.

¹Department of Physics, University of California Berkeley, Berkeley, California 94720, USA. ²Kavli Energy NanoSciences Institute at the University of California Berkeley and the Lawrence Berkeley National Laboratory, Berkeley, California 94720, USA. ³Department of Chemistry, Stanford University Stanford, California 94305, USA. ⁴Materials Sciences Division, Lawrence Berkeley National Laboratory, Berkeley, California 94720, USA. * These authors contributed equally to this work. Correspondence and requests for materials should be addressed to F.W. (email: fengwang76@berkeley.edu).

Signalling and manipulation through the control of electric field distributions is ubiquitous to both biological and physical systems. For example, intercellular electrical activity is central to the signalling and computation of excitable cells such as cardiac and neuronal cells^{1–3}. The voltages generated by bio-electric fields span three orders of magnitude and can fluctuate on the scale of microseconds to hours^{4,5}. Likewise, the generation and manipulation of electric fields inside microscopic channels is the backbone of microfluidics and lab-on-a-chip diagnostics^{6–9}. In the latter applications, electric field gradients are intentionally designed to create strong dielectrophoretic forces, which permit the trapping and control of individual chemical droplets or biological samples along programmable pathways covering hundreds of microns^{10,11}.

Over the past decade, there has been a concerted effort to develop new techniques to observe and analyse the dynamic field fluctuations in liquids, such as the development of multitransistor arrays^{12,13}, voltage-sensitive dyes^{14–18} and new computational paradigms to model^{10,19,20} electric field behaviour. However, it remains an outstanding challenge to achieve label-free, non-perturbative detection with high field sensitivity and high spatio-temporal resolution. For example, the study of network-scale biological activity requires the ability to non-perturbatively record single-cell signals over a large field of view and with sub-millisecond temporal sensitivity. The predominant label-free method of detecting local electric fields across cellular networks are multielectrode and multitransistor arrays^{19,21}. These techniques require prefabricated electrode arrays that are difficult to scale up, are individually amplified, and do not provide the flexibility to measure electrical fields at arbitrary spatial positions. Compared with electrical techniques, optical imaging permits high throughput detection that is compatible with simultaneous complementary measurements. Despite these advantages, there is little research into label-free optical platforms that permit the spatio-temporal detection of electric field²² distributions. Here we address this subset of problems with a critically coupled waveguide-amplified graphene electric field (CAGE) imaging platform, which permits label-free imaging of the dynamics of electric fields in solutions under non-equilibrium conditions.

Results

Design of the CAGE imaging platform. Atomically thin materials like graphene offer exceptional opportunities for electric field sensing due to their unique physical properties and intrinsic sensitivity to their environment. Over the past decade, graphene's optoelectronic properties have been studied extensively^{23,24}. In addition to its distinctive electronic transport properties, graphene couples strongly to light across the visible and the infrared frequency range. A pristine sheet of graphene has a constant absorption of $\pi\alpha \sim 2.3\%$ at all frequencies²⁵. In addition, this absorption can be modulated through electrostatic gating: a gate-induced shift of the Fermi energy that forbids specific optical transitions in graphene due to Pauli blocking (Fig. 1a). We employ this field-dependent optical absorption to achieve highly sensitive and parallel optical detection of local electrical fields.

Realizing this goal requires new optical designs that optimize the detection sensitivity and parallel readout simultaneously. For example, simple transmission mode imaging of gated monolayer graphene yields a 1% change of transmitted light over a gate voltage change of 200 mV around the Pauli blocking region. This results in a voltage sensitivity of only 2 mV, accounting for a typical laser with noise levels of 10^{-4} . However, physical and biological applications require orders of magnitude improvement in voltage sensitivity. To increase the light-matter interaction in graphene, researchers have explored

different approaches such as coupling graphene to silicon waveguides^{26–28}, photonic crystal cavities^{28–30}, plasmon resonances^{31–33} and metamaterials³⁴. These existing methods can improve the voltage sensitivity of optical detection, but are incompatible with parallel detection and imaging.

Here we demonstrate highly sensitive, high-speed optical imaging of local electric field dynamics in solutions using graphene and a critical-coupled planar waveguide. Using a custom numerical simulation, we designed the critically coupled waveguide amplified platform to obtain the so-called critical coupling condition³⁵ where the effective absorption of monolayer graphene approaches 100%. Close to the critical-coupling point, the voltage sensitivity can be enhanced by orders of magnitude. In addition, the planar waveguide permits two-dimensional (2D) time-resolved imaging of the electric field distribution in the solution above graphene. This CAGE imaging achieves a voltage sensitivity down to a few microvolts, a response speed of microseconds, spatial resolution of several microns and highly parallel readout of the dynamics of electrical field distributions.

Figure 1b schematically illustrates the structure of the CAGE imaging platform. Large-area graphene is grown by chemical vapour deposition and transferred to a prism coated with 150 nm of Ta₂O₅ ($n = 2.0856$), forming a high refractive index waveguide. We use an equilateral SCHOTT SF-11 glass (SF-11) prism ($n = 1.743$) with a 1,000 nm top layer of SiO₂ ($n = 1.444$) to evanescently couple a collimated 1.55 μm beam to and from the CAGE sensor. The reflected light is then collected by an infrared objective and imaged onto an InGaAs camera and photodiode.

The concept of waveguide critical coupling is illustrated in Fig. 1c. A collimated s-polarized 1.55 μm incident beam is coupled into the transverse electric (TE) mode of the waveguide at an oblique angle so that condition for total internal reflection is satisfied at the SF-11/SiO₂ and Ta₂O₅/solution interfaces. Under this framework, we can describe the waveguide as a Fabry-Perot cavity with high reflection coefficients $|r_1|$ and $|r_2|$ at the two interfaces, where $|r_1|$ and $|r_2|$ deviate from unity due to the frustrated total internal reflection from the finite SiO₂ thickness at the first interface and the absorption of graphene at the second interface. At resonance coupling, the total reflection R from the Fabry-Perot cavity is described by $R = \frac{(|r_1| - |r_2|)^2}{(1 - |r_1||r_2|)^2}$ (Supplementary Note 1). The value of $|r_2|$ can be varied *in situ* by electrostatic gating of graphene. To attain the highest sensitivity to local electric fields, we gate the graphene to a specific Fermi energy that generates the largest relative change in optical reflection for a given local electric field. At the critical-coupling condition, $|r_1| = |r_2|$ and the total reflection, R , equals zero, at which point all of the light is absorbed by graphene. Consequently, close to the critical coupling condition, the light-graphene interaction is strongly enhanced and the background reflection is very weak contributing to the high voltage sensitivity of CAGE imaging.

High sensitivity via critical coupling. Figure 2a shows the gate-dependent reflectivity response of a typical CAGE detector in a saline solution (blue solid line). The incident 1.55 μm beam is collimated and TE polarized. The resonance condition of the waveguide determines the angle of incident light inside the SF-11 coupling prism to be $\sim 60^\circ$ from normal. With a 1,000 nm SiO₂ layer, the frustrated total internal reflection $|r_1| = 98.2\%$. The reflection coefficient at the Ta₂O₅/solution $|r_2|$ is 97.5% at the charge neutral point ($V_g = -0.14$ V) due to graphene absorption, which leads to a total reflection of $R \sim 1.5\%$. Graphene absorption can be set subsequently by electrostatic gating through the solution. The critical coupling condition $|r_1| = |r_2|$ is realized at $V_g = +0.41$ V (electron doped) and $V_g = -0.69$ V (hole doped), resulting the lowest total reflectivity, R (the residual value of

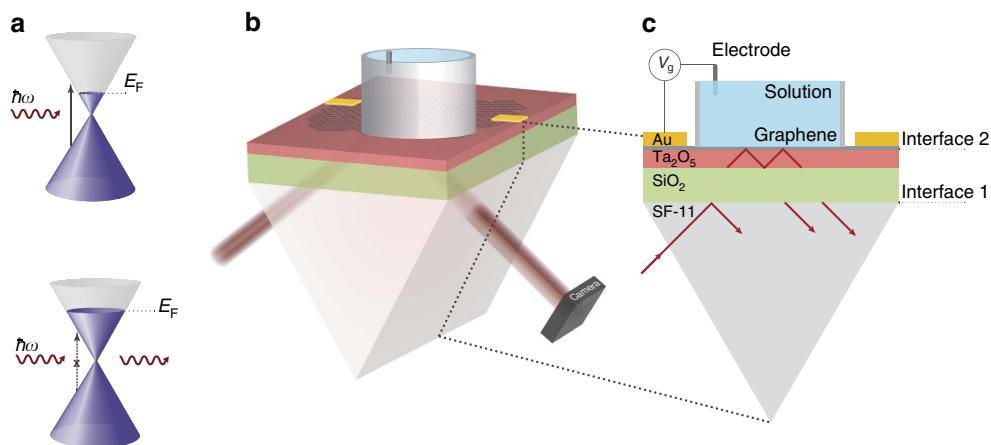


Figure 1 | Graphene optoelectronics and CAGE imaging device. (a) Graphene interband transitions wherein E_F shifts upon gating. The optical modulation is strongest for electronic transitions near the Fermi surface, $2|E_F| = \hbar\omega$, wherein the presence of an external field can shift the Fermi energy and prohibit optical absorption due to Pauli blocking (bottom). (b) CAGE imaging device in which a TE-polarized collimated incident beam at $1.55\ \mu\text{m}$ is coupled through the prism coupler (prism and green layer) into the waveguide (red). Through the waveguide, the beam probes the graphene/solution interface (grey). The critical coupling condition is achieved by varying the incident light angle and by electrostatic gating of graphene through the saline solution (blue). The out-coupled signal is detected by an InGaAs photodiode and/or camera. (c) Cross section of the CAGE imaging platform. Interface 1 and interface 2 form a Fabry-Perot cavity in which we obtain the critical coupling condition. The waveguide-amplified critical coupling condition sets the ratio of light coupling into the waveguide and light absorption at the graphene interface to unity. The optical contrast of local field fluctuations is maximized close to the critical coupling condition, which permits localized and sensitive electric field detection.

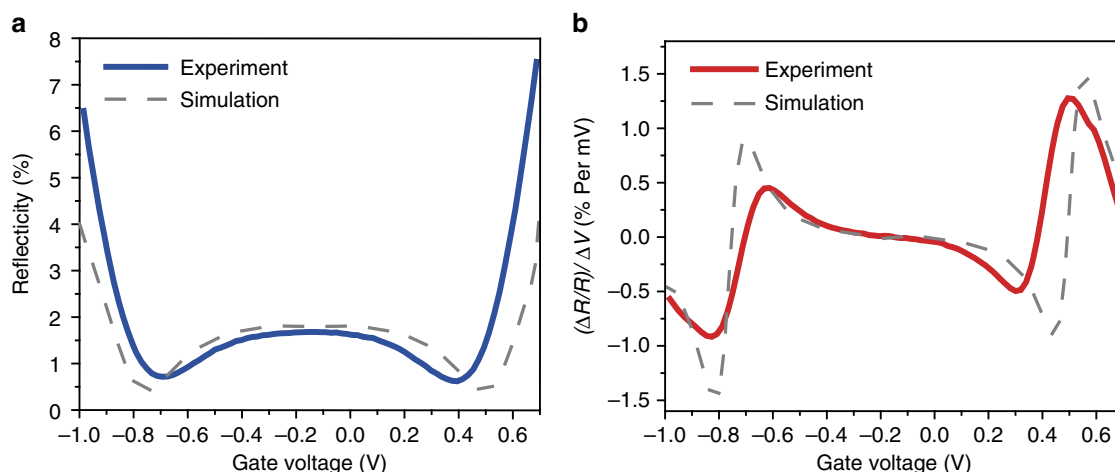


Figure 2 | Optical response characterization of the CAGE sensor. (a) Gate-dependent optical reflectivity of the TE-polarized collimated $1.55\ \mu\text{m}$ beam incident at the waveguide resonance angle. The dip in the optical signal corresponds to the critical coupling condition. The grey dashed line shows the optical response expected from simulation (see text and Supplementary Note 2 for details). (b) CAGE sensor voltage sensitivity, $(\Delta R/R)/\Delta V$, is derived from **a** for both experiment (red) and simulation (grey dashed line). We observe a maximum voltage sensitivity of 1.2% optical change per mV at $V_g = +0.53\ \text{V}$.

$R = 0.63\%$ at critical coupling is due in part to a slight divergence in the incident beam and in part due to defects in the CVD-grown graphene and the waveguide thin film deposition). Further increase of carrier doping leads to a decrease of graphene absorption corresponding to $|r_1| < |r_2|$ and one obtains an increase in total reflectivity. The grey dashed line in Fig. 2a shows the simulated optical response of our device using graphene absorption determined experimentally. (see Supplementary Note 2 and Supplementary Fig. 2 for graphene absorption and Supplementary Note 3 and Supplementary Fig. 3 for simulation details).

The sensitivity of CAGE detection to dynamics of the local electric field is characterized by the relative reflectivity change $\Delta R/R$ caused by a change in voltage induced by the local electric field, ΔV . Figure 2b shows the calculated $(\Delta R/R)/\Delta V$ as a function of the gate voltage from Fig. 2a. CAGE detection is most sensitive

close to the critical coupling condition, where we achieve the greatest optical modulation for a given change in local electric field. For example, a single millivolt of field-induced voltage produces a 1.2% change in reflection at $V_g = 0.53\ \text{V}$. This sensitivity is over 200 times higher than that of the direct transmission configuration ($\sim 1\%$ optical change per 200 mV, Supplementary Note 2). The root-mean-square (RMS) noise of the commercially available 15 mW $1.55\ \mu\text{m}$ butterfly diode lasers is around 0.01% across a 10 Hz–10 kHz bandwidth. Consequently, the CAGE detection permits optical readout of electrical voltages smaller than $10\ \mu\text{V}$ across a wide field of view.

Noise floor and bandwidth. CAGE optical detection of small electric field fluctuations is demonstrated in Fig. 3a. The gate voltage at graphene was set at the highest sensitivity point

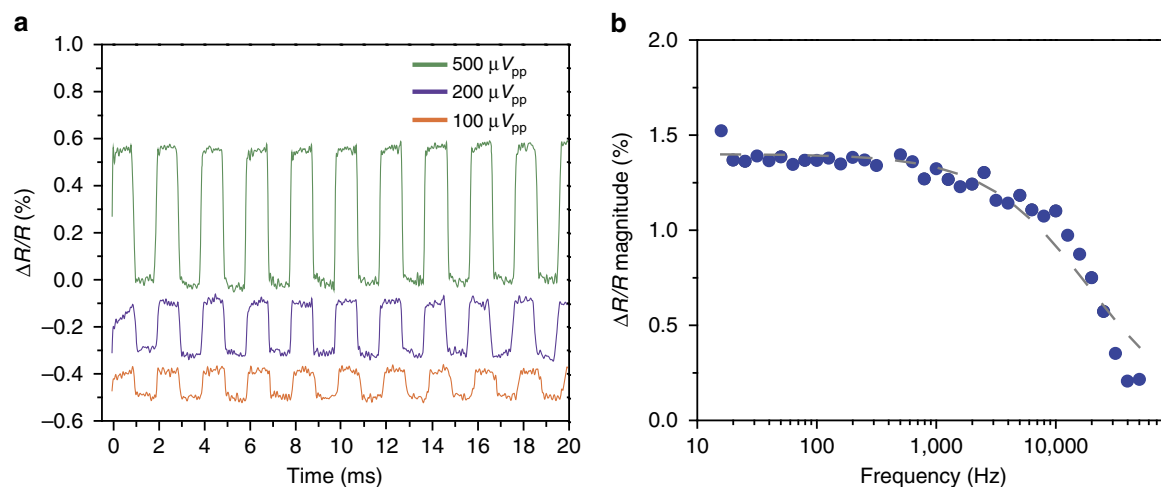


Figure 3 | Voltage sensitivity and temporal bandwidth. (a) Optical detection of an applied modulating voltage. A periodic rectangular waveform is applied with peak-to-peak voltages of $500 \mu V_{pp}$ (green), $200 \mu V_{pp}$ (purple) and $100 \mu V_{pp}$ (orange) with a 10 Hz–10 kHz bandpass filter. The optical response from the $100 \mu V$ applied modulation demonstrates a SNR of 6.5 corresponding to an experimental detection limit of $15 \mu V$. (b) Frequency dependence of the optical signal demonstrating sensitivity to high-speed fluctuations up to 10 kHz. A $1 mV_{pp}$ sinusoidal waveform with frequencies spanning 20 Hz–50 kHz is applied. Shown here for a device with large-area ($80,000 \mu m^2$) graphene. The frequency bandwidth will increase inversely with graphene area as a consequence of graphene's high conductivity. The results provided by an RC equivalent circuit, accounting for the double-layer capacitance and graphene resistance, is plotted as the grey dashed line.

(0.53 V). We applied periodic rectangular pulse sequences with peak voltages ranging from 500 to $100 \mu V$ and recorded the optical readout with a wide band-pass filter from 10 Hz to 10 kHz. The relative reflectivity change is 0.58%, 0.23%, and 0.11% for 500, 200, and $100 \mu V$ voltage pulses, respectively. The results are consistent with the $(\Delta R/R)/\Delta V = 1.2\%$ per mV reported in Fig. 2b. Clear periodic modulation is observed at $V_{pp} = 100 \mu V$ with a signal to noise ratio (SNR) of 6.5. This measurement reflects optical detection capabilities of $\sim 15 \mu V$ or, equivalently, a change of carrier concentration of 2.3×10^8 electrons per cm^2 in graphene. The noise level at 0.017% in Fig. 3a is due to a combination of laser intensity fluctuations and vibrations of optical components. Much higher SNR and therefore higher voltage sensitivity would be possible by improving the optomechanical and laser source stabilities.

The temporal response of CAGE detection is determined by the RC constant of the system, where C is the capacitance of the graphene/electrolyte interface and R is governed by graphene conductance. For local electrical field fluctuations, the effective area and capacitance is small and the response speeds can be very high. Experimentally, we characterized the frequency response of the CAGE detector using a relatively large graphene area (200 by $400 \mu m$), underscoring the applicability of our measurements to large fields of view. Figure 3b shows that the $\Delta R/R$ value remains largely constant up to 10 kHz and decreases at higher frequencies. These measurements yield a 3 dB frequency of 13 kHz (Fig. 3b dashed) and an RC constant of $20 \mu s$. This 10 kHz fast response enables direct observation of electric field dynamics on timescales spanning action potentials^{20,21} and electrophoretic manipulation^{10,11}.

Electric field imaging. Figure 4 demonstrates the capability of CAGE imaging to spatially resolve electric field dynamics. Figure 4a shows a schematic of our experimental set-up. A platinum/iridium microelectrode is placed $5 \mu m$ above the device to create a spatially varying electric field distribution. The spatially resolved reflection from the graphene plane is projected to the image plane using a long working distance near-infrared objective, which we image onto an InGaAs camera.

The spatio-temporal dynamics of local electric fields in solution are captured by the CAGE device at the critical coupling

condition and imaged onto a one-dimensional InGaAs camera array in Fig. 4b,c. A 10 mV electrical pulse with a 200 ms duration is applied at the microelectrode (red waveform Fig. 4b) generating a 1.8 mV local potential at the graphene/solution interface beneath the microelectrode tip (Supplementary Note 4).

The temporal response of the local electric field as a function of position are given as time traces in Fig. 4b. Positions A1, A2 and A3 are increasingly distant from the field source. At position A1, immediately below the excitation electrode, we observe the perturbed reflection intensity due to a fast transient voltage peak that decays in ~ 25 ms to a stationary potential (solid yellow line). As one moves increasingly distant from the field source, the fast transient peak correspondingly reduces (green and blue solid lines). This behaviour matches well with the results of our finite element simulation and may be qualitatively described by the equivalent circuit shown in Supplementary Note 4. This equivalent circuit consists of the solution resistance, impedance from the electrode/solution interface and the impedance from the graphene/solution interface. The results of the calculation using the equivalent circuit are shown as dashed lines in Fig. 4b. The voltage sensitivity is determined by the $\sim 100 \mu V$ RMS noise present before the onset of the excitation; this sets the upper bound of voltage resolution in the one-dimensional camera array.

The complete data set of the local field described above is shown in Fig. 4c. We observe the field dynamics with 5 ms temporal resolution and $100 \mu V$ voltage sensitivity across a full $200 \mu m$. The lower voltage sensitivity in the imaging mode compared with a single InGaAs photodiode is due to the slower speed and a limited dynamic range of our InGaAs array. In the future, the voltage sensitivity and temporal resolution could be extended by adopting a better array detector.

Frames from a CAGE video of local electric field dynamics recorded via an 80 Hz 2D InGaAs camera are shown in Fig. 5. The spatial resolution of our device is on the order of $10 \mu m$ (Supplementary Note 5 and Supplementary Fig. 5). Each frame is normalized by an image taken in zero-field. Compared with the recordings in Fig. 4b, we expect that time $t = -10$ to 0 ms captures the period in which a positive transient voltage emerges and subsequently dissipates away from the excitation microelectrode, and $t = 190$ –240 ms captures the period in which a

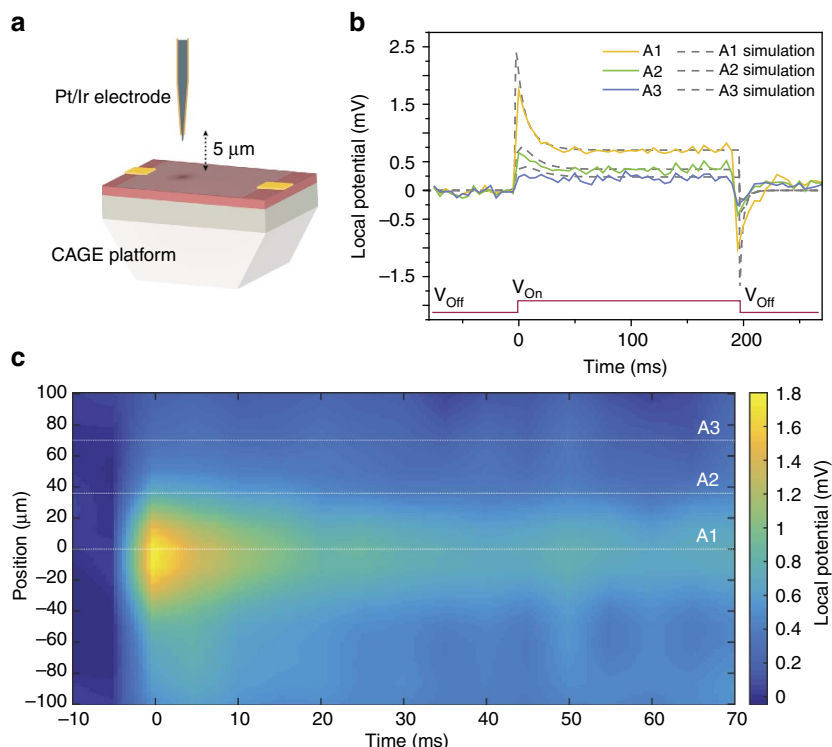


Figure 4 | Detecting local electric field fluctuations with spatial and temporal resolution. (a) Geometry of the experimental set-up in which a waveform is applied to a $2\text{ }\mu\text{m}$ platinum/iridium microelectrode placed in solution $5\text{ }\mu\text{m}$ above the graphene surface of the detector. Applying a waveform to the microelectrode generates a spatially distributed electric field pattern and permits observation of the local electric field modulation in space and time. (b) Temporal dynamics of the experimental (solid) and simulated (dashed) optical CAGE detection of the local electric field at different distances from the local potential source. The local field is generated by a 10 mV 200 ms pulse (red) applied to the microelectrode. The spatial location of A1 (yellow), A2 (green) and A3 (blue) is articulated by white dashed lines in c. (c) CAGE image with spatio-temporal resolution of the first 70 ms of local electric field dynamics described in b projected onto a one-dimensional 193 Hz InGaAs camera. The spatially resolved recording obtains $\sim 100\text{ }\mu\text{V}$ sensitivity with 5 ms temporal resolution.

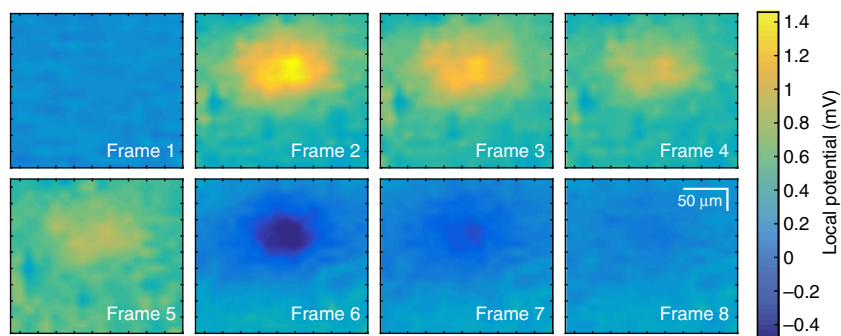


Figure 5 | Images from a single-shot recording in sequence. Still images from the single-shot recording in response to the same pulse in Fig. 4 projected onto a 2D 80 Hz InGaAs camera. Frames 1–4 capture the first 50 ms of the field and its spatial diffusion throughout the solution while frames 5–8 begin at $t = 190\text{ ms}$ and capture the completion of the pulse and its recovery to equilibrium. Frames are separated by 12.5 ms . The reflection intensity in the stills is normalized to that without stimulation.

negative transient voltage recovers to zero. Indeed, the data show that a positive voltage emerges and then diffuses spatially in frames 1–4, and a negative voltage appears and recovers to the equilibrium state in frames 5–8 (Supplementary Note 4). These results demonstrate that dynamic spatial variations of local electric fields can be imaged in real time via the CAGE imaging platform.

Discussion

In summary, we present a method of imaging local electric field dynamics under ambient conditions with high voltage and spatio-temporal resolution through the CAGE imaging platform. This label-free and highly parallel technique offers more than

200-fold improvement over conventional graphene-based optical sensing and resolves sub- $15\text{ }\mu\text{V}$ fluctuations with a bandwidth of 10 kHz across a wide field of view. The CAGE imaging platform is capable of operating under a wide range of chemical and thermal conditions, may be used simultaneously with complementary measurements, and may be spectrally tailored to enable broad applications from improved engineering of lab-on-a-chip devices to sensing bioelectric phenomena across cellular networks.

Methods

Sample preparation. The CAGE imaging structure consists of $1,000\text{ nm}$ SiO_2 (coupling layer) and 150 nm Ta_2O_5 (waveguide layer) deposited on one face of a

1 cm equilateral SF-11 glass prism by ion-assisted deposition. The structure was designed using a custom Python simulation (Supplementary Note 3 and Supplementary Fig. 3) and fabricated by Edmund Optics. A large area graphene film was grown on copper foil using chemical vapour deposition (CVD). A 1 cm² area graphene was transferred onto the waveguide surface by poly(methyl methacrylate) (PMMA) transfer. We obtain high-quality large-area graphene with near-uniform optical absorption at the device/solution interface. The Pt (2 nm)/Au (60 nm) electrodes were deposited on the graphene to make electrical contacts. The metal electrodes were insulated with nitrocellulose lacquer to prevent water-Au chemical reactions during measurements. The device was mounted in a solution chamber printed from PR48 resin (Autodesk), which permits access to the device from both the top and bottom. All data were obtained in a saline solution (155 mM NaCl, 2.966 mM Na₂HPO₄, 1.0588 mM KH₂PO₄) except for imaging data (Figs 4 and 5) obtained in 1 mg l⁻¹ NaCl in water to accommodate the camera's frame rate. An external gate voltage V_g (0.53 V) was applied through a Ag/AgCl electrode in solution to set the Fermi energy of graphene and to test the optical response of CAGE detection under electrostatic gating. For the spatially resolved measurements, an external gate voltage V_g (1.1 V) was applied through the microelectrode, whose high impedance at the electrode/solution interface requires a larger applied voltage but yields the same voltage bias and critical coupling condition at the detector's graphene/solution interface. A 10 mV electrical pulse generates a 1.8 mV local field at the graphene/solution interface beneath the Pt/Ir microelectrode tip (World Precision Instruments, #PTM23B05KTH) (Supplementary Fig. 4b). To this, we applied a small modulation to the micro-positioned microelectrode insulated in parylene with only the final 2 μ m exposed to the solution.

Optical measurements. Supplementary Fig. 1c shows, in detail, the optical set-up used in the study. A stable, 1.55 μ m, 15 mW laser beam is generated by a butterfly telecom laser (Newport Model 708 8-Channel Butterfly) with a current and temperature controller (Newport Model 9016 Modular Controller). The polarization is tuned to the TE direction by a half-wave plate and further cleaned by a calcite polarizer. In the imaging mode, the incident beam is collimated and coupled into the CAGE platform for optimal sensitivity. In the scanning detection mode, the incident beam is controlled with a 17.5 cm focusing lens to have a numerical aperture of 0.002 and selects an area at the graphene interface. The incident light couples into the waveguide from one side of the prism. The prism coated with the planar waveguide is placed on a XY-translational stage and a rotating stage, which allow for fine-tuning of the sample position and incident angle. The reflected light is then collected by a $\times 10$ MPlan objective and sent into an InGaAs 2D camera (Allied Vision Technologies Goldeye 008 SWIR), an InGaAs one-dimensional camera (Andor 1.7 μ m InGaAs DU490A) and into a low-noise InGaAs photodetector, respectively. A circular iris is used to select the probing area for photodiode measurements.

Data availability. The data that support the findings of this study are available from the corresponding author upon request.

References

- Plonsey, R. *Bioelectricity: A Quantitative Approach* (Springer, 2002).
- Cohen, A. E. & Venkatachalam, V. Bringing bioelectricity to light. *Annu. Rev. Biophys.* **43**, 211–232 (2014).
- Yuste, R. From the neuron doctrine to neural networks. *Nat. Rev. Neurosci.* **16**, 487–497 (2015).
- Xie, C., Lin, Z., Hanson, L., Cui, Y. & Cui, B. Intracellular recording of action potentials by nanopillar electroporation. *Nat. Nanotechnol.* **7**, 185–190 (2012).
- Buzsáki, G., Anastassiou, C. A. & Koch, C. The origin of extracellular fields and currents — EEG, ECoG, LFP and spikes. *Nat. Rev. Neurosci.* **13**, 407–420 (2012).
- Gagnon, Z. R. Cellular dielectrophoresis: Applications to the characterization, manipulation, separation and patterning of cells. *Electrophoresis* **32**, 2466–2487 (2011).
- Link, D. R. *et al.* Electric control of droplets in microfluidic devices. *Angew. Chem. Int. Ed.* **45**, 2556–2560 (2006).
- Hunt, T. P., Issadore, D. & Westervelt, R. M. Integrated circuit/microfluidic chip to programmably trap and move cells and droplets with dielectrophoresis. *Lab Chip* **8**, 81–87 (2008).
- Dorfman, K. D., King, S. B., Olson, D. W., Thomas, J. D. P. & Tree, D. R. Beyond gel electrophoresis: microfluidic separations, fluorescence burst analysis, and DNA stretching. *Chem. Rev.* **113**, 2584–2667 (2013).
- Çetin, B. & Li, D. Dielectrophoresis in microfluidics technology. *Electrophoresis* **32**, 2410–2427 (2011).
- Zhang, C., Khoshmanesh, K., Mitchell, A. & Kalantar-zadeh, K. Dielectrophoresis for manipulation of micro/nano particles in microfluidic systems. *Anal. Bioanal. Chem.* **396**, 401–420 (2010).
- Lambacher, A. *et al.* Electrical imaging of neuronal activity by multi-transistorarray (MTA) recording at 7.8 μ m resolution. *Appl. Phys. A* **79**, 1607–1611 (2004).

- Hutzler, M. *et al.* High-resolution multitransistor array recording of electrical field potentials in cultured brain slices. *J. Neurophysiol.* **96**, 1638–1645 (2006).
- Lavis, L. D. & Raines, R. T. Bright ideas for chemical biology. *ACS Chem. Biol.* **3**, 142–155 (2008).
- Li, L. Fluorescence probes for membrane potentials based on mesoscopic electron transfer. *Nano Lett.* **7**, 2981–2986 (2007).
- Park, J. *et al.* Screening fluorescent voltage indicators with spontaneously spiking HEK cells. *PLoS ONE* **8**, e85221 (2013).
- Miller, E. W. *et al.* Optically monitoring voltage in neurons by photo-induced electron transfer through molecular wires. *Proc. Natl. Acad. Sci. USA* **109**, 2114–2119 (2012).
- Park, K., Deutsch, Z., Li, J. J., Oron, D. & Weiss, S. Single molecule quantum-confined stark effect measurements of semiconductor nanoparticles at room temperature. *ACS Nano* **6**, 10013–10023 (2012).
- Einavoll, G. T., Kayser, C., Logothetis, N. K. & Panzeri, S. Modelling and analysis of local field potentials for studying the function of cortical circuits. *Nat. Rev. Neurosci.* **14**, 770–785 (2013).
- Angle, M. R., Cui, B. & Melosh, N. A. Nanotechnology and neurophysiology. *Large-Scale Rec. Technol.* **32**, 132–140 (2015).
- Spira, M. E. & Hai, A. Multi-electrode array technologies for neuroscience and cardiology. *Nat. Nanotechnol.* **8**, 83–94 (2013).
- Wang, Y. *et al.* Imaging local electric field distribution by plasmonic impedance microscopy. *Anal. Chem.* **88**, 1547–1552 (2016).
- Nair, R. R. *et al.* Fine structure constant defines visual transparency of graphene. *Science* **320**, 1308–1308 (2008).
- Wang, F. *et al.* Gate-variable optical transitions in graphene. *Science* **320**, 206–209 (2008).
- Mak, K. F., Ju, L., Wang, F. & Heinz, T. F. Optical spectroscopy of graphene: from the far infrared to the ultraviolet. *Explor. Graphene Recent Res. Adv.* **152**, 1341–1349 (2012).
- Liu, M. *et al.* A graphene-based broadband optical modulator. *Nature* **474**, 64–67 (2011).
- Koester, S. J. & Li, M. Waveguide-coupled graphene optoelectronics. *IEEE J. Sel. Top. Quantum Electron.* **20**, 84–94 (2014).
- Majumdar, A., Kim, J., Vuckovic, J. & Wang, F. Electrical control of silicon photonic crystal cavity by graphene. *Nano Lett.* **13**, 515–518 (2013).
- Shiue, R.-J. *et al.* Enhanced photodetection in graphene-integrated photonic crystal cavity. *Appl. Phys. Lett.* **103** (2013).
- Gan, X. *et al.* Strong enhancement of light-matter interaction in graphene coupled to a Photonic crystal nanocavity. *Nano Lett.* **12**, 5626–5631 (2012).
- Grigorenko, A. N., Polini, M. & Novoselov, K. S. Graphene plasmonics. *Nat. Photon* **6**, 749–758 (2012).
- Chen, J. *et al.* Optical nano-imaging of gate-tunable graphene plasmons. *Nature* **487**, 77–81 (2012).
- Fei, Z. *et al.* Gate-tuning of graphene plasmons revealed by infrared nanoimaging. *Nature* **487**, 82–85 (2012).
- Lee, S. H., Choi, J., Kim, H.-D., Choi, H. & Min, B. Ultrafast refractive index control of a terahertz graphene metamaterial. *Sci. Rep.* **3**, 2135 (2013).
- Liu, Y. *et al.* Approaching total absorption at near infrared in a large area monolayer graphene by critical coupling. *Appl. Phys. Lett.* **105** (2014).

Acknowledgements

The authors thank Felix Alfonso, Hui-Ling Han, Sufei Shi and Zhiwen Shi for helpful discussions and thank Andreas Bastian and the Ember Team at Autodesk for help designing and printing the device mount and solution holder. This work was supported by the National Science Foundation grant DMR-1344302 (optical measurements, simulations, device fabrication), and by the U.S. Department of Energy Office of Basic Energy Sciences contract no. DE-AC02-05CH11231 Nanomachine program (graphene fabrication). F.W. and B.C. acknowledge support from the David and Lucile Packard fellowship. H.B.B. acknowledges support from the NSF Graduate Research Fellowship (grant DGE 1106400). A.F.M. acknowledges support from the Stanford Bio-X Graduate Fellowship.

Author contributions

F.W. and B.C. conceived of the experiment. J.H. and H.B.B. contributed equally to this work. J.H., H.B.B. and F.W. designed the experiment. H.-Z.T., P.R.F. and M.F.C. grew high-quality CVD graphene. J.H. and H.B.B. developed the simulations, fabricated the devices, built the optical set-up, performed the optical measurements and wrote the manuscript. J.H., H.B.B. and A.F.M. analysed the data. All authors contributed to the discussion of the results and to the manuscript.

Additional information

Supplementary Information accompanies this paper at <http://www.nature.com/naturecommunications>

Competing financial interests: The authors declare no competing financial interests.

Reprints and permission information is available online at <http://npg.nature.com/reprintsandpermissions/>

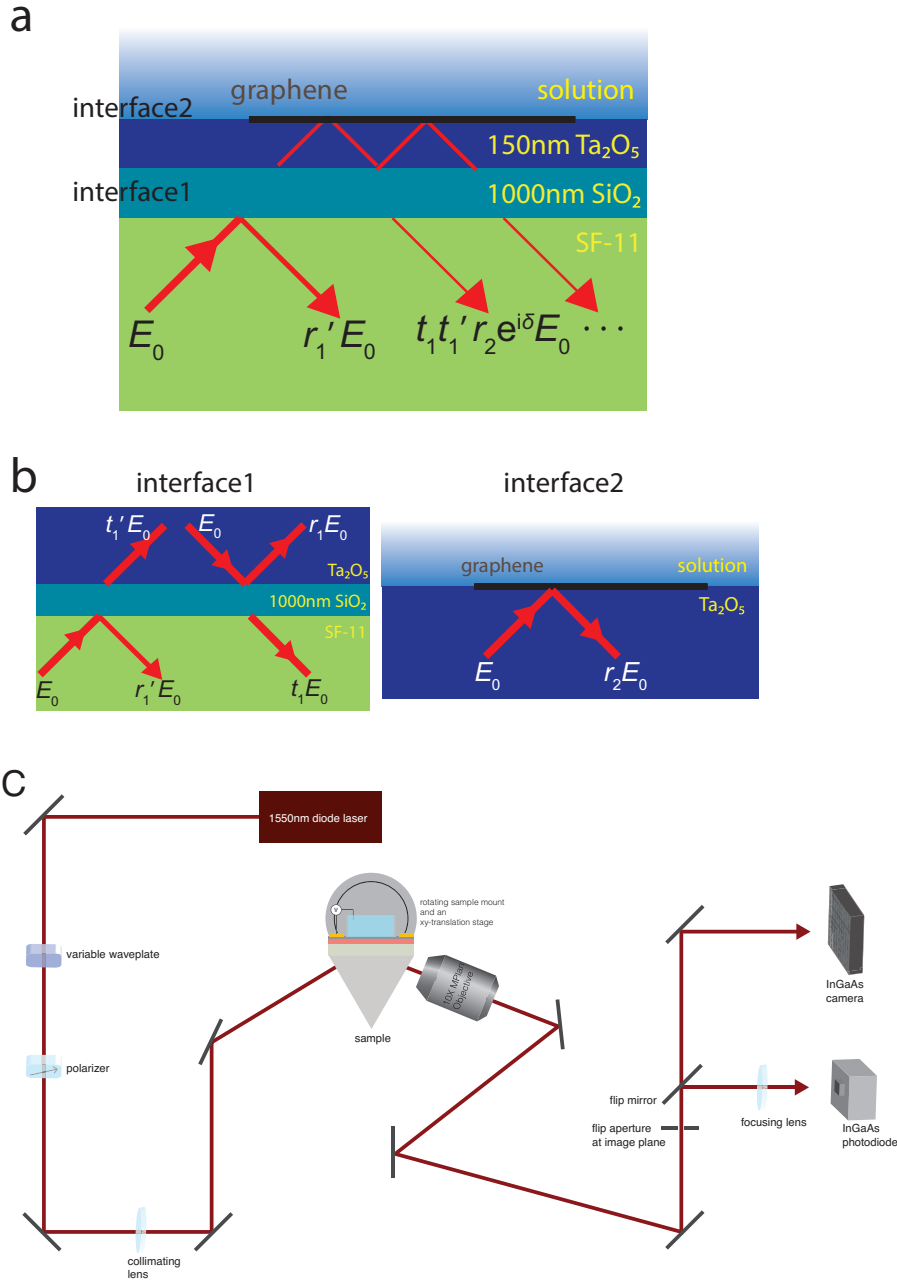
How to cite this article: Horng, J. *et al.* Imaging electric field dynamics with graphene optoelectronics. *Nat. Commun.* 7, 13704 doi: 10.1038/ncomms13704 (2016).

Publisher's note: Springer Nature remains neutral with regard to jurisdictional claims in published maps and institutional affiliations.

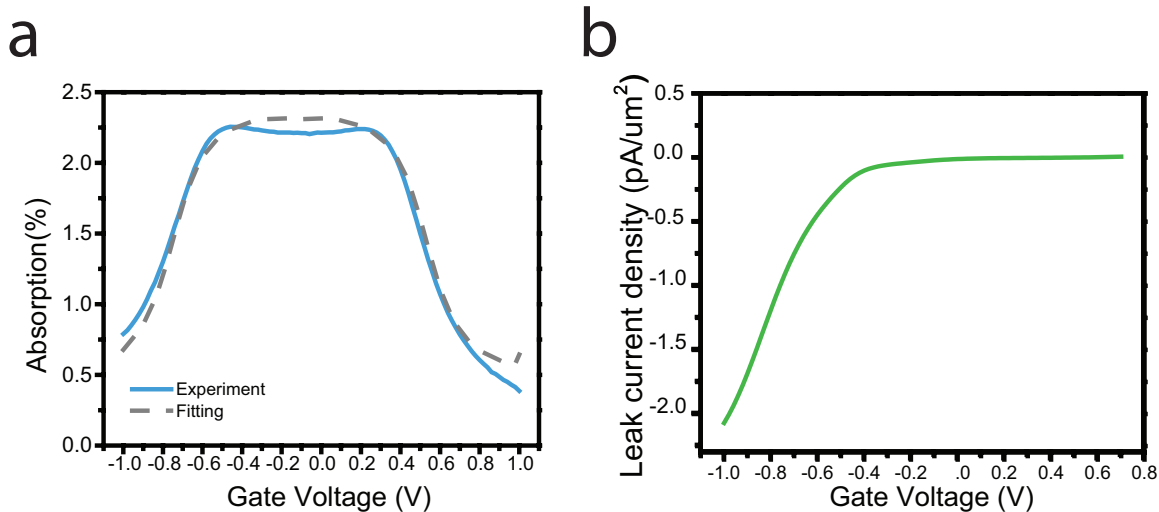


This work is licensed under a Creative Commons Attribution 4.0 International License. The images or other third party material in this article are included in the article's Creative Commons license, unless indicated otherwise in the credit line; if the material is not included under the Creative Commons license, users will need to obtain permission from the license holder to reproduce the material. To view a copy of this license, visit <http://creativecommons.org/licenses/by/4.0/>

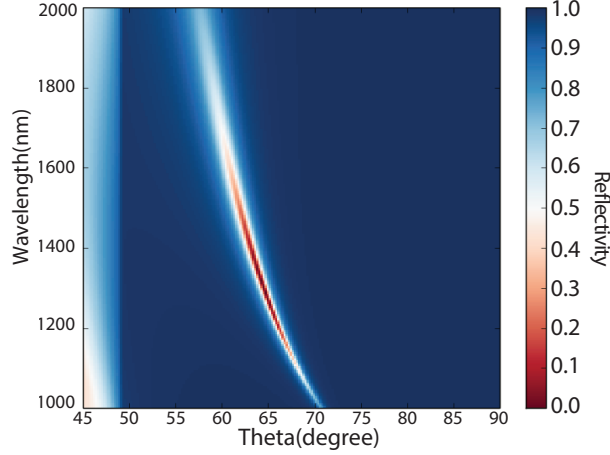
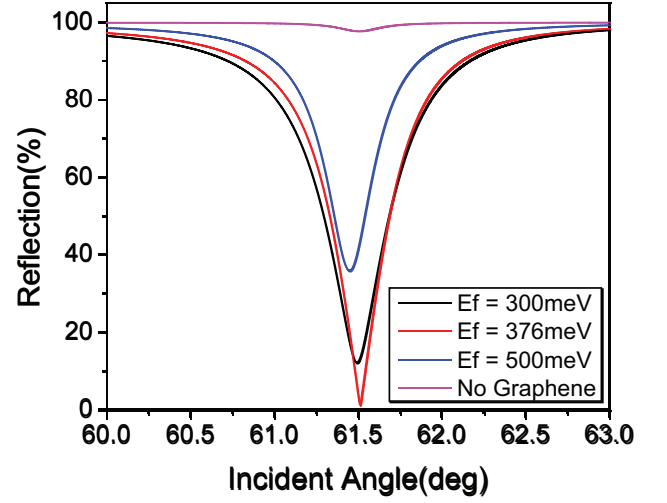
© The Author(s) 2016



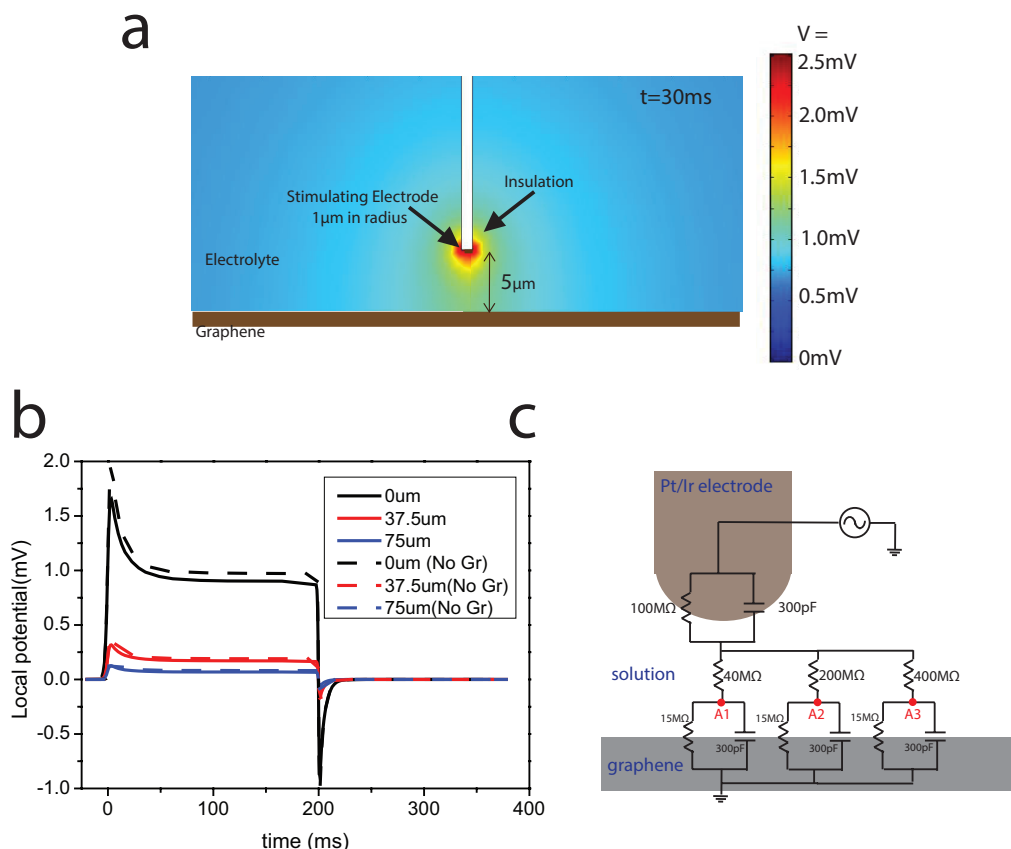
Supplementary Figure 1| Detailed analysis on the critically coupled waveguide structure. **a**, The geometry of the layered structure are shown (not in scale) with the multiple reflection analysis. Interface1 and interface2 are highly reflective and form a Fabry-Perot cavity. The definition of r_1', r_2, t_1, t_1' are given in **(b)** and in the text. **b**, Two sub-systems considered in S1: interface1 consists SF11/SiO₂(1000 nm)/Ta₂O₅ and interface2 consists Ta₂O₅/Graphene/water. Both of them form a highly reflecting mirror. **c**, Schematic of optical setup.



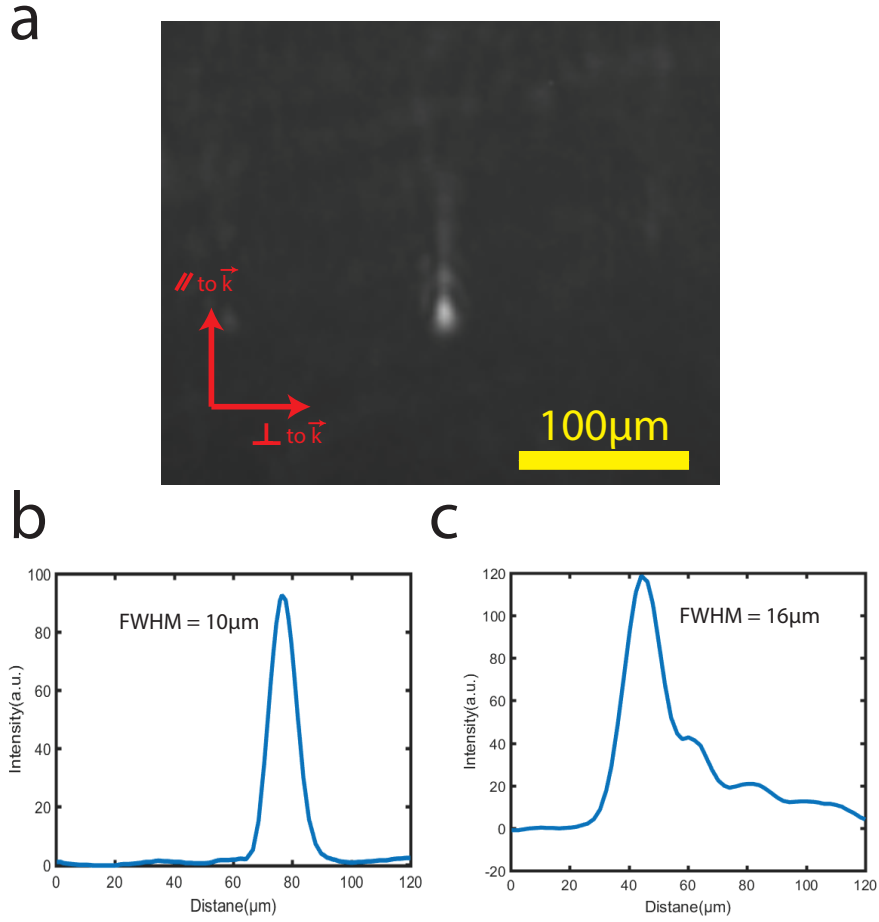
Supplementary Figure 2 | Gate dependence of optical absorption of monolayer graphene. **a**, Optical absorption measurement with a monolayer graphene on glass substrate at $1.55\mu\text{m}$ at normal incidence as a function of gate voltage via Ag/AgCl electrode through saline solution. **b**, Simultaneous current density measurement on graphene electrodes while during voltage scan in Supplementary Figure 2a. The current density is very small within the window of $\pm 1\text{V}$, indicating negligible chemical reaction between graphene and PBS solution.

a**b**

Supplementary Figure 3 | Simulation of optical response from the graphene optoelectronic electric field imaging device. a, Reflectance map of s-polarized planewaves with varying wavelengths and incident angles from the device structure illustrated in Figure 1b in the main text. Reflectance is reduced due to absorption of graphene only when the incident angle matches with 0th TE mode of the waveguide. **b,** Reflectance as a function of incident angles for different graphene Fermi energy. The depth of resonance dip can be controlled by tuning graphene's Fermi energy via an external gate.



Supplementary Figure 4 | Finite-element simulation for microelectrode voltage modulation. **a**, Cross-section of simulation geometry and simulated potential distribution in solution at $t = 30$ ms. **b**, Dynamics of local potential (solid) in electrolyte just above graphene for positions corresponding to A1 (below the tip), A2 (37.5 μm away) and A3 (75 μm away). The same quantity without graphene is also shown as a grey dashed line. The simulation gives a qualitative description for the spatio-temporal phenomenon seen in experiment and indicates that our device acts a nonperturbative local field detector. **c**, An equivalent circuit may be used to describe the spatio-temporal dynamics in our experimental configuration.



Supplementary Figure 5 | Calibration of spatial resolution of CAGE imaging system.
a, Image of one microsphere with 1 μm diameter taken with CAGE optical system. **b**, Intensity profile on a line cut across the direction perpendicular to the light propagation direction (\vec{k}). Spatial resolution in this direction is 10 μm . **c**, Intensity profile on a line cut across the direction parallel to \vec{k} . The spatial resolution in this direction is 16 μm .

Supplementary Note 1: Description of critically coupled waveguide

Supplementary figure 1a shows a detailed analysis of the waveguide structure and describes the working principle of the device. To describe the interaction of the light with the multilayer device, we can separate the system into two sub-systems: one consists of SF11/SiO₂(1000 nm)/Ta₂O₅ and other consists Ta₂O₅/Graphene/solution as each of them form a highly reflecting surface. The sub-systems are shown in supplementary figure 1b. Supplementary figure 1c outlines the optical imaging setup.

The SF11/SiO₂(1000 nm)/Ta₂O₅ sub-system can be treated by standard methods of frustrated total internal reflection(FTIR). Here, we assume the reflection and transmission coefficients for light incident from the SF11 side are r'_1 and t'_1 , while the coefficients from the Ta₂O₅ side are r_1 and t_1 . One can prove that $|r_1| = |r'_1|$ and $t_1 t'_1 = (1 - |r_1|^2) \exp(\delta_1 + \delta'_1 + \pi)$ ¹, where δ_1 and δ'_1 are the phase of r_1 and r'_1 , respectively.

In the Ta₂O₅/Graphene/water sub-system, r_2 is defined as the reflection coefficient for light incident from the Ta₂O₅ side of the interface. r_2 can be calculated with the Fresnel equation and perturbation theory on graphene absorption

$$r_2 = 1 - A_{gr} \times Re \left[\frac{(1 + r_2^0)^2}{r_2^0} \right] = 1 - A_{gr} \times 1.66$$

where A_{gr} is the absorption of graphene, and r_2^0 is reflection coefficient at interface of Ta₂O₅/water without graphene.

We can now consider the optical properties of the combined system. As these two sub-systems are highly reflective, the combined structure consists of two parallel highly reflected mirrors and may therefore be described as a Fabry-Perot cavity. The total reflected radiation E_r is the interference of the multiple reflections and has the form:

$$\begin{aligned} \frac{E_r}{E_0} &= r'_1 + t_1 t'_1 r_2 e^{i\delta} \left[1 + (r_1 r_2 e^{i\delta}) + (r_1 r_2 e^{i\delta})^2 + \dots \right] \\ &= r'_1 + \frac{t_1 t'_1 r_2 e^{i\delta}}{1 - r_1 r_2 e^{i\delta}} \quad (\text{Supplementary Equation 1}) \end{aligned}$$

where E_0 is the incident electric field, $e^{i\delta}$ the phase accumulation as the light propagates through the Ta₂O₅ medium. Given the relationship between r_1, r'_1, t_1, t'_1 , supplementary equation 1 may be simplified to

$$\frac{E_r}{E_0} = e^{i\delta'} \frac{|r_1| - |r_2| e^{i\Delta}}{1 - |r_1| |r_2| e^{i\Delta}} \quad (\text{Supplementary Equation 2})$$

where $\Delta = \delta + \delta_1 + \delta_2$ is the round trip phase accumulation in the waveguide. The resonance of the Fabry-Perot cavity takes place at $e^{i\Delta} = 1$, which is the same requirement for the zeroth mode for Ta₂O₅ planar waveguide.² The phase accumulation, Δ , depends sensitively on the incident angle, allowing one to find the resonance of the Fabry-Perot cavity by varying the incident angle coupling into the waveguide structure. By squaring the supplementary equation 2, one can get the reflectance formula shown in Eq1 in the text and the critical condition $|r_1| = |r_2|$, at which the reflection intensity dramatically decreases as the light has near-100% absorption into graphene (see main text for further discussion). Operating the device at the critical coupling condition can enhance the contrast significantly due to the strongly enhanced light-matter interaction and the low reflection background.

Supplementary Note 2: Optical absorption of monolayer graphene

To optimize the optical response of the CAGE device, we first examined the gate dependence of graphene's optical absorption in an ionic solution (see methods). We obtained an optical reflection measurement from monolayer graphene on glass substrate at 1.55 μm with normal incidence as a function of gate voltage through solution with a Ag/AgCl electrode. The absorption is derived from the reflection data based on Fresnel equations and shown in supplementary figure 2a. The absorption at zero-gate voltage is measured to be 2.19%, which is close to the universal optical absorption of graphene (2.3% theoretically). The absorption starts to decrease at around $\pm 0.4\text{V}$ due to the band-filling effect and continues to decrease to $\pm 1.0\text{V}$. The absorption may be tuned from 0.47% to 2.19% over a gate voltage of $\pm 1.0\text{V}$.

The optical absorption of graphene, A_{gr} , contains contributions from both interband and intraband transitions in graphene. Its frequency dependence at different Fermi energies (E_{F}) can be approximated by^{3,5}

$$A_{\text{gr}}(E_{\text{F}}) = \frac{\pi e^2}{\hbar c} \left[1 + \frac{1}{\pi} \left(\tan^{-1} \frac{E - 2|E_{\text{F}}|}{\Gamma} - \tan^{-1} \frac{E + 2|E_{\text{F}}|}{\Gamma} \right) \right] + \frac{4e^2}{\hbar c \tau} \frac{|E_{\text{F}}|}{E^2 + (1/\tau)^2}$$

(Supplementary Equation 3)

where E is the incident photon energy, Γ , the interband and $1/\tau$ the intraband transition broadening, respectively. The Fermi level E_{F} varies with the carrier concentration, n , as $E_{\text{F}} = \hbar v_{\text{F}} \sqrt{\pi n}$, where the Fermi velocity v_{F} is $1.1 \times 10^6 \text{ m s}^{-1}$. In the electrolytic cell, the averaged carrier concentration, n_0 , can be described by a capacitor model $n_0 = C(V_{\text{g}} - V_{\text{CNP}})/e$, where C is the double layer capacitance of the solution under Ag/AgCl gating, and V_{CNP} , the charge neutral point, is fitted to be -0.11V .

To account for the doping inhomogeneity in graphene, we introduce a local carrier concentration broadening of $\Delta = 5 \times 10^{11} \text{ cm}^{-2}$. As a result, the conductivity of graphene can be described as

$$A_{\text{gr}}(n_0) = \frac{\int A_{\text{gr}}(n) e^{-(n-n_0)^2/\Delta^2} dn}{\int e^{-(n-n_0)^2/\Delta^2} dn} \quad (\text{Supplementary Equation 4})$$

The fitting results for the graphene absorption as a function of V_{g} are plotted in supplementary figure 2a (dashed line), where the fitted parameters both interband and

intraband broadening are 80meV, double layer capacitance $C = 2.07 \mu F cm^{-2}$. From the absorption curve of graphene, we estimate that the voltage sensitivity in a transmission configuration $(dT/T)/dV = 0.0048\%$ per mV due to intrinsic broadening of graphene interband transitions. The current density on graphene electrodes is monitored during the optical measurement and shown in supplementary figure 2b. The current is small within the window of $\pm 1V$ and the band-filling effect can be reproduced many times indicating a lack of a chemical reaction between graphene and the solution.

Supplementary Note 3: Simulation of optical response from device

To optimize the device structure, we built a custom Python simulation that explored materials, dimensions, tolerances, and coupling conditions to provide theoretical bounds on spatial resolution and field sensitivity. The simulation is based on transfer-matrix formalism. These simulated conditions included polarization and coupling angle of the infrared beam, graphene's optical properties in aqueous solutions, and the structure of planar waveguide layers. Drawing upon these results we found the optimal parameters, compatible with standard fabrication techniques, for the spatial and charge sensitivity. Supplementary figure 3a shows the reflection map of s-polarized planewaves with various wavelength of light and incident angles from a graphene-coated waveguide structure shown in Fig. 1b. in the main text. Most of the wavelength and incident angle combinations give unity reflection due to total internal reflection. Only when the incident angle matches the zeroth transverse electric mode (TE mode), can light couple into the waveguide and absorption by graphene becomes significant.

Supplementary figure 3b shows the reflection of s-polarized planewaves at 1.55 μm from the same waveguide structure as a function of incident angles for different graphene Fermi energies. The dips in the reflection curves are due to the zeroth transverse electric mode of the waveguide and the depth of resonance peak changes significantly for different Fermi energies of graphene. The optical absorption of graphene decreases monotonically with the Fermi energy and determines the fraction of light being absorbed in the waveguide. The simulation indicates that the strongest (deepest) resonance takes place at one specific Fermi energy (376 meV in supplementary figure 3b). At this Fermi energy, the absorption of graphene is such that the multiple reflections in the waveguide destructively interfere, resulting in a near-zero reflection of the probe beam.

Finally, we simulate optical response in a real experimental setting where the incident angle is fixed at the resonance condition and assuming numerical aperture N.A. = 0.002 by averaging the reflectance within the angle divergence ($\sim 0.6^\circ$). The absorption of graphene used in the simulation is taken from the experimental data from supplementary figure 2a. The simulated voltage-dependent reflectance and sensitivity of

the device is shown in Figure 2a and 2b in the main text as dashed lines, respectively, and may be compared with the experimental responses from the CAGE optical system.

Supplementary Note 4: Finite-element simulation of the microelectrode voltage modulation

To understand the spatio-temporal behavior of local potential measured in micro-electrode stimulation experiment shown in Fig. 4a in the main text, we use the Electrochemistry Module in COMSOL Multiphysics to simulate the electric potential in solution during applied voltage pulses. The simulation accounts the effect of the electrode kinetics in addition to solution resistance. The current distribution in electrolyte is assumed to obey Ohm's law and the electrode interface are simulated by a double-layer capacitance together with a linearized Butler–Volmer equation to describe electrode current, namely:

$$i_{el} = i_0 \frac{\alpha F}{RT} \eta \quad (\text{Supplementary Equation 5})$$

where i_{el} is the electrode current, i_0 the exchange current density, α the cathodic and anodic charge transfer coefficient, F the faraday constant, R the gas constant, T the temperature and η the overpotential of the electrode.

In the simulation, we use a 1 μm -radius-disk stimulating electrode with $C = 10\text{F m}^{-2}$, $i_0 = 20\text{A m}^{-2}$, $\alpha = 1$ embedded in an electrolyte with conductivity $\sigma = 0.0022\text{ S m}^{-1}$. The parameters for stimulating electrode are provided by the manufacturer and electrolyte conductivity is from literature.⁶ Large-area graphene is set 5 μm away from the stimulating electrode and with parameters: $C = 0.02\text{F m}^{-2}$ and $i_0 = 0.05\text{ A m}^{-2}$. The capacitance and exchange current density for graphene are estimated from the absorption measurement in supplementary figure 2a and leak current measurement in supplementary figure 2b, respectively. At $t=0$, both graphene and stimulating electrode are set at 0 V, after which a 200 ms pulse with 10 mV magnitude is applied to the stimulating electrode to simulate the experiment described in Figure 4c of the main text. The cross-section of simulation geometry is shown in supplementary figure 4a. The color map in supplementary figure 4a shows the simulated spatial distribution of electrolyte potential at $t = 30\text{ ms}$ during the voltage pulse applied.

Supplementary figure 4b shows the voltage dynamics in solution just above graphene for three positions corresponding to A1 (below the tip), A2(37.5 μm away) and A3(75 μm away). The simulated local potential dynamics can be compared with the data

observed in Fig. 4c and Fig. 4d of the main text and provides a qualitative description for the spatio-temporal phenomenon observed in experiment.

The potential difference with graphene (solid lines) and without graphene (dashed lines) are shown in supplementary figure 4b. The potential difference is within 10%, indicating that the solution and probe are essentially blind to the presence of graphene, and that our detection schema may be treated as a truly nonperturbative readout of local electric fields.

The dynamics of the electric potential in solution can also be qualitatively described by the equivalent circuit shown in supplementary figure 4c. This equivalent circuit consists of the solution resistance, impedance from the electrode/solution interface, and impedance from the graphene/solution interface. The results of the calculation using the equivalent circuit are shown as dashed lines in Figure 4c.

Supplementary Note 5: Spatial resolution of CAGE imaging scheme

To demonstrate the spatial resolution of our CAGE imaging system, we spread polystyrene microspheres (with a 1 μm diameter) on the waveguide surface and analyzed the images formed by a single microsphere. Figure S5a shows an image of one microsphere taken with the CAGE optical system. The objective we use in the study is 10X MPlan objective with N.A. = 0.26. The resulting lower limit for spatial resolution is 7 μm , which is larger than the diameter of a polystyrene microsphere, therefore the microsphere can be treated as a point source and the intensity profile reports the point spread function of the optical system.

Supplementary figure 5b shows a intensity profile on a line cut across the direction perpendicular to the light propagation in the waveguide, \vec{k} . The full width at half maximum(FWHM) is measured to be 10 μm , which is reflective of the spatial resolution in this direction. Supplementary figure 5c shows a intensity profile on a line cut across the direction parallel to \vec{k} . We observe a long tail of ~ 40 μm in the \vec{k}_{\parallel} direction. This is due to the slow decay of light over the waveguide propagation distance. The reflection coefficient of the waveguide depends sensitively on the incident angle. As the focused beam has a finite angular spread due to the uncertainty principle, interference is observed as the multiple secondary peaks observed in the \vec{k}_{\parallel} direction. With graphene as absorber and our designed waveguide structure, we estimate that the light decays in the tens of microns length scale which corroborates with the experimental observation. Despite the decay tail, the spatial resolution in the propagation direction determined by the FWHM is 16 μm .

Supplementary References

1. Zhu, S., Yu, A. W., Hawley, D. & Roy, R. Frustrated total internal reflection: A demonstration and review. *Am. J. Phys.***54**, 601–607 (1986).
2. Jackson, J.D., *Classical electrodynamics 3rd edition* 385 (Wiley India Pvt. Limited, 2007).
3. Wang, F. *et al.* Gate-Variable Optical Transitions in Graphene. *Science* **320**, 206–209 (2008).
5. Horng, J. *et al.* Drude conductivity of Dirac fermions in graphene. *Phys Rev B* **83**, 165113 (2011).
6. Haynes, W. M. & Lide, D. R. *CRC handbook of chemistry and physics : a ready-reference book of chemical and physical data* D-221 (CRC Press, 2011).
7. Einevoll, G. T., Kayser, C., Logothetis, N. K. & Panzeri, S. Modelling and analysis of local field potentials for studying the function of cortical circuits. *Nat Rev Neurosci***14**, 770–785 (2013).